Flux-closure domains in high aspect ratio electroless-deposited CoNiB nanotubes

M Staňo, Sandra Schaefer, Alexis Wartelle, Maxime Rioult, Rachid Belkhou, Alessandro Sala, Tevfik Onur Menteş, Andrea Locatelli, Laurent Cagnon, Beatrix Trapp, et al.

Imaging magnetic flux-closure domains and domain walls in electroless-deposited CoNiB nanotubes

M. Staňo,[1,*] S. Schaefer,[2] A. Wartelle,[1] M. Rioult,[3] R. Belkhou,[3] A. Sala,[4] T. O. Menteş,[4] A. Locatelli,[4] L. Cagnon,[1] B. Trapp,[1] S. Bochmann,[5] S. Martin,[1,6] E. Gautier,[6] J. C. Toussaint,[1] W. Ensinger,[2] and O. Fruchart[1,6,†]

[1] *Univ. Grenoble Alpes, CNRS, Institut NEEL, F-38000 Grenoble, France*
[2] *Technische Universität Darmstadt, D-64287 Darmstadt, Germany*
[3] *Synchrotron SOLEIL, Saint-Aubin BP 48, F-91192 Gif-sur-Yvette, France*
[4] *Elettra - Sincrotrone Trieste S.C.p.A., I-34149 Basovizza, Trieste, Italy*
[5] *Friedrich-Alexander University of Erlangen-Nürnberg, D-91058 Erlangen, Germany*
[6] *Univ. Grenoble Alpes, CNRS, CEA, SPINTEC, F-38000 Grenoble, France*

(Dated: April 21, 2017)

Magnetic nanotubes are predicted to host magnetic domains and domain walls with a topology different from that for flat elements[1, 2]. Compared to cylindrical nanowires, reports on magnetism of isolated metallic nanotubes are scarce and so far no material has given rise to well-defined magnetic domains. Here we report the fabrication of high-aspect ratio CoNiB nanotubes by electroless plating inside a porous template. Through imaging, we evidenced multiple magnetic domains and domain walls in these nanotubes. Surprisingly, magnetization in the domains is orthoradial (azimuthal, *vortex-like*), a situation not anticipated by theory for long nanotubes. The material is therefore technologically appealing for a dense 3D magnetic device such as the racetrack memory[3] (based on shifting magnetic walls), as flux-closure domains should efficiently prevent cross-talk related to internal dipolar fields. Further, we show tuning of a growth-induced anisotropy and thus of the magnetic state of the tube by annealing.

In nanomagnetism and spintronics, magnetic domain wall (DW) motion has been considered mainly in flat strips prepared by lithography[4, 5]. However, magnetic nanotubes and cylindrical nanowires fabricated in vertical arrays by bottom-up methods are more suitable for a design of 3D devices containing a large amount of elements. After decades of experiments on cylindrical nanowire arrays, the focus is now shifting to single-nanowire physics based on transport[6], magnetometry[7], and imaging[8] involving the first experimental confirmations of DWs[9, 10]. These wires could provide a model situation for DW motion under magnetic field[11] or spin-polarized current[12].

Magnetic nanotubes, less exploited in comparison to the simple nanowire geometry, have been reported mainly in the context of biomedicine[13] and catalysis[14], while their individual magnetic properties have been largely overlooked. Yet theory and simulations predict similar physics of DWs in nanotubes compared to cylindrical nanowires[15, 16], including DW motion without Walker instabilities[17]. Their potential for new physics and devices is also higher than that of nanowires. Indeed, their magnetic properties can be tuned by changing the tube wall thickness, and more complex architectures can be prepared based on core-shell structures[18], analogous to multilayers in 2D spintronics. Besides, curvature-related effects have also been predicted such as an effective Dzyaloshinskii-Moriya interaction[2] or the non-reciprocity of spin-wave propagation[19]. Last but not least, unlike in case of nanowires, no magnetic singularities (Bloch points) can be present on the tube axis [15], which facilitates the numerical modelling.

In the case of tubes, the main bottleneck lies in the development and reliable fabrication of magnetic materials with suitable structural quality. Several fabrication methods exist, mostly utilizing templates, i.e. filling nanopores or coating nanopillars. Electroplating can yield tubes with diameters as small as 25 nm[20] and good material quality, but wire-vs-tube growth instabilities occur[21]. Atomic layer deposition[22] provides a great control over the tube wall thickness, but the resulting material, oxide, is quite granular and magnetically imperfect[18]. Single magnetic structures prepared by rolling thin sheets (micrometric diameters)[23] or a physical deposition on vertical hexagonal pillars[24] have been recently investigated. The geometry is however not a pure tube for the former, while the latter cannot be up-scaled to a dense array due to shadowing effects.

Here we present $(Co_{80}Ni_{20})B$ nanotubes prepared by conformal electroless plating[14, 25] as detailed in the Methods. This technique provides good control over the tube wall thickness, diameters down to 50 nm[26], and high quality material. After discussing briefly the tube microstructure, we first detail the imaging of magnetic domains and DWs in our tubes, then we identify the DW configuration based on a comparison with simulations. Later we discuss the anisotropy giving rise to the observed domains (and walls). Further, we show that we can tune the anisotropy and thus the magnetic state of these tubes by annealing, making them a versatile building block unlocking new physics and devices based on nanotubes.

* michal.stano@neel.cnrs.fr
† olivier.fruchart@cea.fr

In this work we consider tubes with diameter 300−400 nm, length 30 µm and tube wall thickness approximately 30 nm. The tubes are nanocrystalline (Fig. 1a,b) with a complex microstructure (Fig. 1c,d): 1-2 nm thick boundaries rich in lighter elements (oxygen detected, probably also boron is concentrated here), separate 10 nm grains, themselves displaying an internal structure at the scale of 2 nm (more in Supplementary II A-B). Similar microstructure, with *macrograins* embedded in a boron-rich matrix, has been already reported in case of NiB nanoparticles[27].

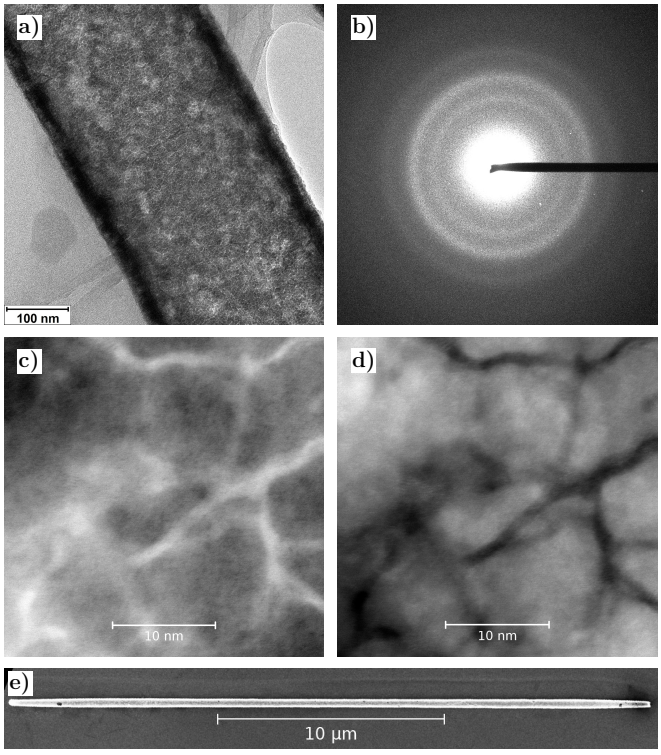

Fig. 1. **Structure of electroless-deposited CoNiB nanotubes**. a) Transmission electron microscopy image of a nanocrystalline CoNiB tube and b) corresponding selected area (240 nm in diameter) electron diffraction pattern showing diffusive rings originating from nanograins with all possible crystallographic orientations. c) Closer look on the grains with scanning transmission electron microscopy in bright and d) dark field (Z contrast, heavier elements appear brighter). e) Scanning electron microscopy image of the whole tube.

In order to image magnetic domains and DWs in the tubes, we use X-ray Magnetic Circular Dichroism - PhotoEmission Electron Microscopy (XMCD-PEEM). This photon-in, electron-out technique maps the component of magnetization parallel to the X-ray beam propagation direction. We use the so-called shadow geometry on single (isolated) tubes dispersed on a doped Si substrate, as pioneered by Kimling et al.[18] and further developed in our group[28]. This method provides information about magnetization both on the tube surface and in the tube volume. The latter is inferred from the photoelectron signal in the tube shadow, which reflects the magnetization-dependent dichroic X-ray transmission through the sample.

Fig. 2a displays an XMCD-PEEM image of two orthogonal tubes. Surprisingly, the magnetic contrast is insignificant for the tube aligned parallel to the X-ray beam direction, while being maximum when the beam is transverse to the tube axis. This shows that magnetization is not axial as expected from theory for long soft magnetic tubes[16], but it is perpendicular to the tube axis. Examination of the shadow reveals an inversion of contrast for X-rays having gone through the top and bottom parts of the tube (Fig. 2b), whereas uniform transverse magnetization would give rise to a monopolar contrast[28]. This proves that magnetization is not

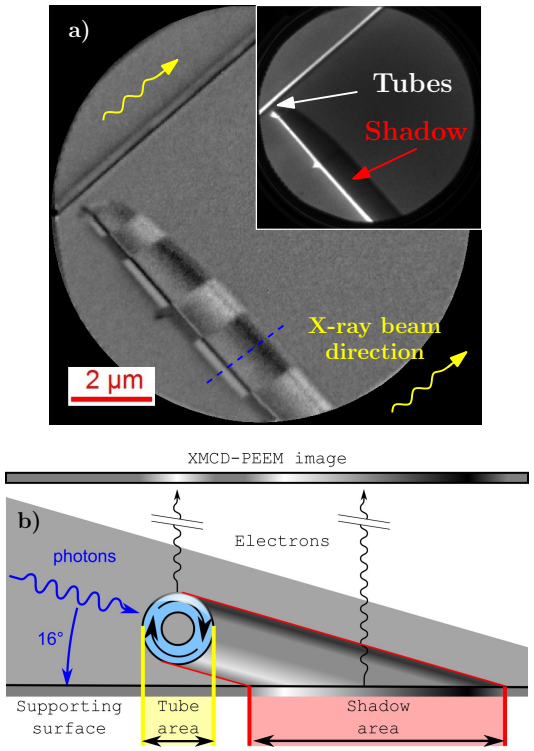

Fig. 2. **Magnetic orthoradial flux-closure domains.** a) XMCD-PEEM (Co-L_3 edge) image of two orthogonal tubes. The tube along the beam (top) gives rise to almost zero contrast, whereas strong contrast is observed for the tube perpendicular to the beam, revealing domains with orthoradial magnetization. The grey line in the shadow close to the rim comes from oxidation of the inner tube surface (nonmagnetic). The inset shows a non-magnetic photoemission electron microscopy image of the tubes. b) Scheme with the orthoradial magnetization and XMCD-PEEM contrast corresponding to a line profile of an orthoradial domain marked by a blue, dashed line in a). Note that in the experiment the tubes lie on the substrate and only part of the shadow can be observed; further the scheme is valid only for L_3 edges of 3d metals. Sometimes contrast inversion can be seen also in the tube area as detailed in[28].

uniformly transverse in the tubes but orthoradial, curling around the tube axis. Similar contrast patterns have

been reported for curling in nanowires[8, 10]. Note that the tube is multidomain: the sense (sign) of the circulation of the flux-closure alternates along the tube axis. Such tubes would be of interest for devices like racetrack memory (Fig. 3) as flux-closure domains reduce the interaction between neighbouring elements.

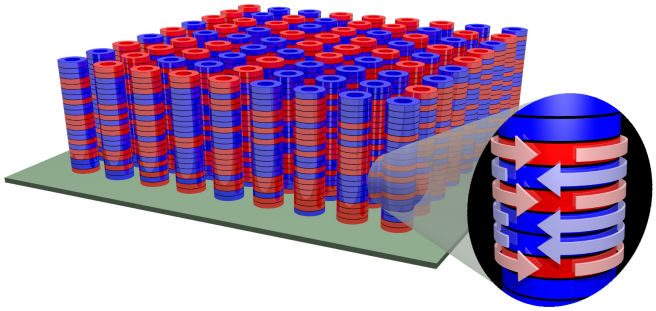

Fig. 3. **Scheme of tubular racetracks.** Bits of information are coded by orthoradial domains with opposite circulation of magnetization. Flux-closure domains significantly reduce the stray field and thus the cross-talk in a dense array of tubes in a potential memory device.

Additionally, we study how the magnetization behaves between the adjacent orthoradial domains. This information, namely the DW type and structure, is the key to determine the ability of a DW to be displaced by magnetic field and more important by spin-transfer torques[29]. A simple view of DWs between orthoradial domains can be obtained by imagining the tube unrolled into a flat strip. Two successive orthoradial domains with opposite circulation turn into a thin film with in-plane magnetization and a 180° DW parallel to magnetization in the domains (Supplementary Fig. 6). As was noticed by Sun[16], we may expect DWs of Bloch (radial magnetization) or Néel type (axial magnetization), named in analogy to thin films.

In order to determine the DW configuration, we probed the tubes with X-ray beam both along and perpendicular to their axis and compared experimental images with a numerical modelling based on micromagnetic simulations and XMCD-PEEM post-processing (see Methods). No XMCD contrast is seen with the beam parallel to the tubes, from which we exclude Néel DWs (axial magnetization). Therefore, DWs should be of the Bloch type. This is consistent with the images for the beam now perpendicular to the tube axis, which display a tilted domain boundary on the tube itself (Fig. 4a,b). The tilt is caused by magnetization in the Bloch DW changing direction from parallel to antiparallel to the X-ray beam when going from the front to the back side of the tube surface. In majority of the cases, the tilt is in the same direction. This together with the alternation of the domains implies that the neighbouring Bloch walls have opposite polarity - radial magnetization pointing inwards or outwards (Supplementary III C). An additional magnetic flux-closure would thus appear between neighbouring DWs.

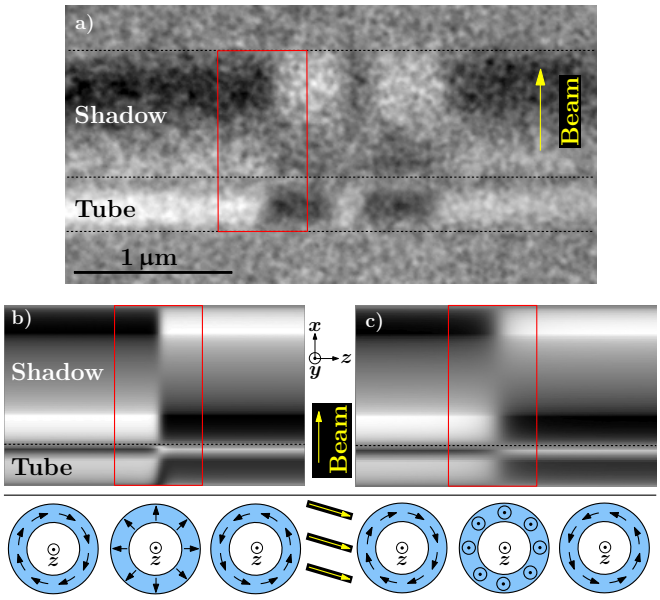

Fig. 4. **Domain walls between flux-closure domains.** a) Experimental XMCD-PEEM with the beam perpendicular to the tube featuring 5 orthoradial domains, the red rectangle highlights an area with one domain wall. We compare this DW to a simulated contrast for b) Bloch and c) Néel walls. Schematic tube cross-sections below the simulations show the magnetization in domains and the domain wall (in the middle of the tube) respectively. Note that in the experiment part of the shadow is covered by the structure itself.

For the magnetic racetrack, ideal DWs should not have a net magnetic charge. First, this would reduce the interaction among elements in densely-packed arrays. Second, it is expected that DWs with no net charge are narrower. While our Bloch walls do have some dipolar charge, they are quite narrow compared to Néel walls (Supplementary Fig. 6) and DWs in between domains with longitudinal (axial) magnetization.

Let us now turn to the reason for orthoradial magnetization. We find very similar domains following either AC-field demagnetization along the transverse direction, or saturation along the tube axis. Therefore the orthoradial curling seems to be the ground state for this material and geometry. Recently, Wyss and coworkers[24] observed with XMCD-PEEM CoFeB and NiFe nanotubes (around 300 nm in diameter, 30 nm tube wall thickness, formed by sputtering on semiconducting nanowires with a hexagonal cross-section). They found the curling (*global vortex*) only for tubes shorter than 1-2 µm (our tubes have 20-30 µm); longer tubes displayed axial magnetization with the curling only at the tube ends as expected from the theory[16]. Similarly, our tubes should display axial magnetization (Supplementary III A). Therefore we argue that an additional contribution, magnetic anisotropy, has to be present to promote alignment of magnetization in the orthoradial direction.

We determined experimentally the strength of the

anisotropy field promoting the orthoradial magnetization. We used scanning transmission X-ray microscopy under external magnetic field to image the magnetic state of single tubes; around 25 mT were required to bring the magnetization from orthoradial to axial. This corresponds to an effective anisotropy constant of $10\,\mathrm{kJ/m^3}$ (Supplementary IV B). Hysteresis loops obtained by magnetometry on both arrays of tubes still in a template and on single tubes on a Si substrate provide very similar values (Supplementary II C). This suggests that the anisotropy originates from the growth itself, and is not caused by liberating the tubes from the matrix or laying them on the substrate.

As regards the microscopic reason for the anisotropy, we can rule out a magneto-crystalline contribution, because of the nanocrystalline nature of the material (see Fig. 1a,b). Possible scenarios include inter-grain surface magnetic anisotropy and magneto-elastic coupling (inverse magnetostriction) associated with a curvature-related anisotropy effects lifting the degeneracy between the orthoradial and axial directions. Both phenomena may provide an anisotropic contribution to magnetic energy due to anisotropic strain, or an anisotropic grain size or shape. In both cases, the anisotropy values are compatible with the experiment (Supplementary IV C).

For comparison we also considered nanocrystalline tubes with very similar geometry but from $(Ni_{80}Fe_{20})B$. These proved to be axially magnetized (Supplementary V). The difference between the two materials is the strength of the magnetostriction, which is sizeable and negative for $(Co_{80}Ni_{20})B$[30] (also Supplementary Tab. I), and nearly vanishing and positive for $(Ni_{80}Fe_{20})B$[30].

In order to investigate the role of the granular structure or the strain in the observed orthoradial anisotropy, we annealed the tubes at various temperatures and examined their magnetization state after cooling to room temperature. As can be seen in Fig. 5, the XMCD contrast associated with the orthoradial domains becomes weaker and finally disappears with the increasing annealing temperature. Orthoradial magnetization persists only at the ends of some tubes (e.g. Fig. 5, left tube), as expected from the locally high demagnetizing field[16]. We attribute the loss of the contrast to a gradual rotation of magnetization towards the axial direction (more in Supplementary VI B). The final weak uniform contrast is determined by the close-to-perpendicular direction of longitudinal magnetization with respect to the beam direction. Note that the degree of the transformation is not the same for all tubes for a given temperature (Fig. 5), possibly due to a slightly different tube wall thickness. Moreover, above 450°C some tubes exhibit defects - mainly holes (Supplementary Fig. 10). These imperfections translate also into inhomogeneities in the magnetic configuration.

The expected reduction of strain and the grain growth upon annealing are both consistent with the reduction of the orthoradial anisotropy.

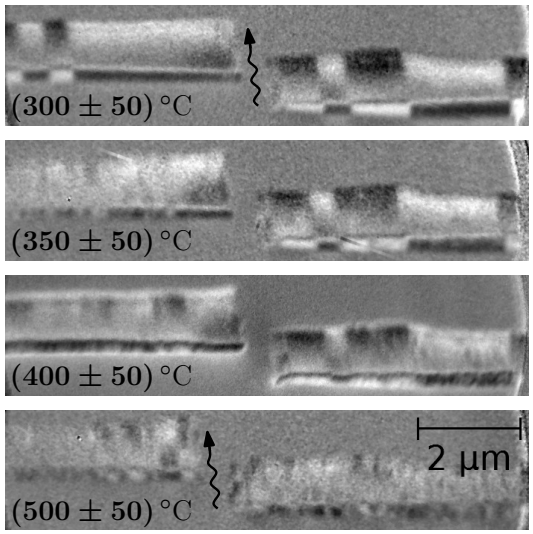

Fig. 5. **Changing the magnetic anisotropy upon gradual annealing of the tubes**. XMCD-PEEM images (same contrast range [-13%..13%]) of the same tubes after annealing at increasing temperature. All images are taken after cooling down to room temperature. X-ray beam arrives close to perpendicular to the tube axis as indicated by the arrow. With the increasing annealing temperature, the orthoradial magnetization pattern becomes weaker and gradually disappears, persisting only close to the tube extremity (end curling). The degree of the transformation is not the same for both tubes, probably due to a different tube wall thickness. After remagnetization along the tube axis (bottom image), both tubes display close to uniform contrast in the shadow, a sign of magnetization pointing along the tube axis. The contrast (bottom image) is weak due to a very small component of the magnetization along the beam.

In conclusion, we synthesized nanocrystalline CoNiB nanotubes by electroless plating in porous templates. Magnetic imaging revealed series of well-defined domains with orthoradial magnetization separated by Bloch-type walls. The orthoradial anisotropy may originate from the growth-induced strain and/or grain shape, while its strength can be tailored through annealing or material composition. This new material offers a versatile playground to search for the peculiar physics of spin-waves and domain-wall motion predicted in magnetic nanotubes. In terms of technology, flux-closure domains generate weak and very short-ranged stray fields, while being separated by narrow (Bloch-like) domain walls. Such tubes are therefore more promising than wires with axial magnetization to serve in the 3D racetrack memory due to reduced dipolar cross-talk in a dense array and for a good vertical packing density. More generally, the development of a 3D spintronics based on core-shell nanotubes, as a counterpart of multilayer thin-film technology, may be at hand.

METHODS

Sample preparation

Fabrication. CoNiB tubes were prepared by electroless deposition inside porous ion track-etched polycarbonate membranes (lab-made, Supplementary I B) with an average pore diameter around 300 nm and length 30 microns.

At first, the porous template is sensitized with a $SnCl_2$ solution and activated with a $PdCl_2$ solution[25]. After three cycles of sensitization plus activation, the template is washed with ethanol and water, then immersed in the electroless plating bath for 20 min at room temperature. The NiCo aqueous plating solution consists of 100 mM $NiSO_4 \cdot 7H_2O$, 30 mM $CoSO_4 \cdot 7H_2O$, 100 mM sodium citrate dihydrate, and 100 mM dimethylamine borane. Further information can be found in Supplementary I A-C.

Preparation for measurements. After the deposition, washing and drying of the template, the metallic film deposited on the top and bottom surfaces of the polymeric template is removed by a gentle mechanic polishing using a sand paper. For measurements requiring single (isolated) tubes, the polycarbonate template is dissolved in dichloromethane and the tubes are rinsed several times with the same solvent. Depending on the measurement technique, the tubes are dispersed either on a doped Si substrate with alignment marks (for XMCD-PEEM or focused magnetooptics/Kerr), or on a Cu grid with a thin lacey carbon film (for transmission electron microscopies) or on a 100 nm-thick SiN membrane (for scanning transmission X-ray microscopy).

X-ray Magnetic Circular Dichroism microscopies

X-ray PhotoEmission Electron Microscopy (X-PEEM)

X-PEEM[31, 32] was used for all tube images featured in the main text. The sample is irradiated with a monochromatic X-ray beam arriving 16° from the substrate plane, with illumination size of several tens of microns. Excited photoelectrons are collected by PEEM from both sample surface and shadow area on the substrate (the latter arising from X-rays partially transmitted through the sample)[18]. Thanks to the grazing incidence of the beam, the resolution in the shadow is increased roughly by a factor of 3.6 ($1/\sin 16°$) along the beam direction. The energy of photons is tuned to the L_3 absorption edge of cobalt (around 778 eV). Circular magnetic dichroism, a difference in absorption of circularly left and circularly right polarized X-rays, leads to a difference in the photoelectron yield. The resulting contrast is related to the projection of magnetization along the beam direction. In the shadow area, which reflects volumic information integrated along the photon path, the situation is more complex and may require modelling[28]. The spatial resolution is around 30-40 nm for the magnetic imaging. The magnetic field was applied in situ using a dedicated sample cartridge with a coil below the sample. Due to the collection of electrons, the technique is implemented under ultra-high vacuum.

Scanning Transmission X-ray Microscopy (STXM)

This technique relies on the transmission of circularly polarized X-rays through a thin sample that must be placed on a thin, X-ray transparent substrate (100 nm-thick SiN membrane in our case). The X-ray beam is focused by diffractive Fresnel zone plate optics to a spot of 30 nm. Scanning by the sample (on piezo-stage) is performed in order to construct an image, pixel by pixel. Magnetic imaging relies again on XMCD at Co-L_3. The contrast is very similar to the one obtained with XMCD-PEEM in the shadow. However, as this technique involves only photons, imaging under significant magnetic field is possible. We used STXM to obtain images of CoNiB under increasing axial magnetic field to extract the strength of the anisotropy field related to the orthoradial anisotropy. The magnetic field is applied thanks to a set of 4 permanent magnets whose orientation is controlled by motors. The setup enables application of magnetic field up to 200 mT. The imaging was conducted under primary vacuum (imaging under secondary vacuum or even atmospheric pressure is possible).

More information on both techniques can be found in a review by Fisher & Ohldag[33] or book by Stöhr & Siegmann[34].

Annealing

The in-situ annealing was performed under ultra-high vacuum, however in a chamber distinct from the X-PEEM microscope chamber. We ramped the temperature to the desired value, keeping it at least for 30 min (except for the first one, 300°C - only 10 min), and then we cooled the sample down to room temperature. The annealing was repeated several times with gradual increase in the target annealing temperature. The imaging was performed after each annealing step. The temperature control was not very precise as we used a small current-heated filament below the sample. The temperature was estimated based on previous and similar filament heating experiments, and on a comparison with annealing of twin samples in more controlled environment. This also implies a rather large uncertainty of ±50 °C.

Simulations

For the micromagnetic simulations we used FeeLLGood[35, 36], a home-built code based on a temporal integration of the Landau-Lifshitz-Gilbert

equation in a finite-element scheme, i.e., using tetrahedra as elementary cells. First, we compute the micromagnetic configuration of nanotubes with two opposite orthoradial domains separated by either a Bloch-like or Néel-like DW. The initial state for these DWs is pure radial (Bloch-like wall) and axial (Néel-like wall) magnetization between the domains. The simulated distributions of magnetization were later post-processed to model shadow XMCD-PEEM contrast[28].

For computational reasons and for the sake of qualitative comparison, we simulated nanotubes with smaller diameter than the experimentally-investigated ones. This implies the use of higher effective anisotropy than in the experiment to stabilize the orthoradial magnetization. No qualitative difference is expected for larger tubes - this was checked for tubes with diameter 120 nm and tube wall thickness 30 nm (Supplementary Fig. 6).

The micromagnetic simulation parameters follow: spontaneous induction $\mu_0 M_s = 1.0\,\mathrm{T}$ ($1.0 \pm 0.2\,\mathrm{T}$ determined from magnetometry on the electroless CoNiB thin films deposited on a flat Si substrate), and exchange stiffness $A = 13\,\mathrm{pJ/m}$. Geometrical parameters: tube diameter 50 nm (smaller than experiment), tube wall thickness 10 nm, length 400 nm (magnetic charges at tube ends removed - mimicking very long tube), and the tetrahedron size was 3 nm or smaller.

The orthoradial anisotropy is imposed by defining the axial direction as a hard axis with an uniaxial anisotropy constant. $K = -50\,\mathrm{kJ/m^3}$ and $K = -100\,\mathrm{kJ/m^3}$ were used for Néel-like DW and Bloch-like DW, respectively. The value deduced from the experiment on larger tubes (diameter around 300 nm) is of the order of $-10\,\mathrm{kJ/m^3}$ (determined from an equivalent anisotropy field extracted from STXM under field on single tubes, magnetometry on sparse array of tubes as well as focused Kerr on individual tubes - see Supplementary II C, IV B).

Shadow-XMCD contrast arising from the relaxed magnetic configuration was derived using a dedicated modelling and a numerical implementation[28]. Having performed the experiment at Co-L_3 edge, we assume the X-ray linear absorption coefficients μ to be those for pure cobalt multiplied by the atomic fraction of cobalt in the tube material. We disregard the boron influence and also suppose that Ni absorption at the Co-L_3 edge is negligible as we are well below the Ni-L absorption edges. Namely we used $\mu_+ = 0.038\,\mathrm{nm^{-1}}$ and $\mu_- = 0.064\,\mathrm{nm^{-1}}$ for two opposite circular polarizations of the X-ray beam (data for pure elements extracted from Nakajima's work[37]).

[1] Hertel, R. Curvature-induced magnetochirality. *Spin* **03**, 1340009 (2013). URL http://dx.doi.org/10.1142/S2010324713400092.

[2] Streubel, R. *et al.* Magnetism in curved geometries. *J. Phys. D: Appl. Phys.* **49**, 363001 (2016). URL http://stacks.iop.org/0022-3727/49/i=36/a=363001.

[3] Parkin, S. S., Hayashi, M. & Thomas, L. Magnetic domain-wall racetrack memory. *Science* **320**, 190–194 (2008).

[4] Thomas, L. & Parkin, S. *Current induced domain-wall motion in magnetic nanowires*, vol. 2 - Micromagnetism of *Handbook of Magnetism and Advanced Magnetic Materials*, chap. Magnetic configurations in small elements, magnetization processes and hysteretic properties (John Wiley & Sons, 2007). URL http://dx.doi.org/10.1002/9780470022184.hmm210.

[5] Parkin, S. & Yang, S.-H. Memory on the racetrack. *Nat. Nanotechnol.* **10**, 195–198 (2015).

[6] Wegrowe, J.-E., Kelly, D., Franck, A., Gilbert, S. E. & Ansermet, J.-P. Magnetoresistance of ferromagnetic nanowires. *Phys. Rev. Lett.* **82**, 3681–3684 (1999). URL http://link.aps.org/doi/10.1103/PhysRevLett.82.3681.

[7] Wernsdorfer, W. *et al.* Nucleation of magnetization reversal in individual nanosized nickel wires. *Phys. Rev. Lett.* **77**, 1873 (1996).

[8] Bran, C. *et al.* Spin configuration of cylindrical bamboo-like magnetic nanowires. *J. Mater. Chem. C* **4**, 978–984 (2016). URL http://dx.doi.org/10.1039/C5TC04194E.

[9] Biziere, N. *et al.* Imaging the fine structure of a magnetic domain wall in a Ni nanocylinder. *Nano Lett.* **13**, 2053–2057 (2013).

[10] Da Col, S. *et al.* Observation of Bloch-point domain walls in cylindrical magnetic nanowires. *Phys. Rev. B* **89**, 180405 (2014).

[11] Thiaville, A. & Nakatani, Y. *Domain-wall dynamics in nanowires and nanostrips*, 161–205 (Springer Berlin Heidelberg, Berlin, Heidelberg, 2006). URL http://dx.doi.org/10.1007/10938171_5.

[12] Yan, M., Kákay, A., Gliga, S. & Hertel, R. Beating the Walker limit with massless domain walls in cylindrical nanowires. *Phys. Rev. Lett.* **104**, 057201 (2010).

[13] Son, S. J., Reichel, J., He, B., Schuchman, M. & Lee, S. B. Magnetic nanotubes for magnetic-field-assisted bioseparation, biointeraction, and drug delivery. *J. Am. Chem. Soc.* **127**, 7316–7317 (2005).

[14] Li, X.-Z., Wu, K.-L., Ye, Y. & Wei, X.-W. Controllable synthesis of Ni nanotube arrays and their structure-dependent catalytic activity toward dye degradation. *CrystEngComm* **16**, 4406–4413 (2014).

[15] Usov, N., Zhukov, A. & Gonzalez, J. Domain walls and magnetization reversal process in soft magnetic nanowires and nanotubes. *J. Magn. Magn. Mater.* **316**, 255–261 (2007).

[16] Sun, C. & Pokrovsky, V. L. Magnetic properties of a long, thin-walled ferromagnetic nanotube. *J. Magn. Magn. Mater.* **355**, 121 – 130 (2014). URL http://www.sciencedirect.com/science/article/pii/S0304885313009049.

[17] Yan, M., Andreas, C., Kákay, A., García-Sánchez, F. & Hertel, R. Fast domain wall dynamics in magnetic nanotubes: Suppression of Walker breakdown and Cherenkov-like spin wave emission. *Appl. Phys. Lett.* **99**, 122505 (2011).

[18] Kimling, J. *et al.* Photoemission electron microscopy of three-dimensional magnetization configura-

tions in core-shell nanostructures. *Phys. Rev. B* **84**, 174406 (2011). URL http://link.aps.org/doi/10.1103/PhysRevB.84.174406.

[19] Otálora, J. A., Yan, M., Schultheiss, H., Hertel, R. & Kákay, A. Curvature-induced asymmetric spin-wave dispersion. *Phys. Rev. Lett.* **117**, 227203 (2016). URL http://link.aps.org/doi/10.1103/PhysRevLett.117.227203.

[20] Wang, X. W., Yuan, Z. H. & Fang, B. C. Template-based synthesis and magnetic properties of Ni nanotube arrays with different diameters. *Mater. Chem. Phys.* **125**, 1–4 (2011).

[21] Fukunaka, Y., Motoyama, M., Konishi, Y. & Ishii, R. Producing shape-controlled metal nanowires and nanotubes by an electrochemical method. *Electrochem. Solid State Lett.* **9**, C62–C64 (2006).

[22] Daub, M., Knez, M., Goesele, U. & Nielsch, K. Ferromagnetic nanotubes by atomic layer deposition in anodic alumina membranes. *J. Appl. Phys.* **101**, 09J111 (2007).

[23] Streubel, R. *et al.* Retrieving spin textures on curved magnetic thin films with full-field soft X-ray microscopies. *Nat. Commun.* **6** (2015).

[24] Wyss, M. *et al.* Imaging magnetic vortex configurations in ferromagnetic nanotubes. *arXiv:1701.01685* (2017). URL https://arxiv.org/abs/1701.01685.

[25] Schaefer, S. *et al.* NiCo nanotubes plated on Pd seeds as a designed magnetically recollectable catalyst with high noble metal utilisation. *RSC Adv.* **6**, 70033–70039 (2016).

[26] Mertig, M., Kirsch, R. & Pompe, W. Biomolecular approach to nanotube fabrication. *Appl. Phys. A* **66**, S723–S727 (1998).

[27] Geng, J., Jefferson, D. A. & Johnson, B. F. Exploring the structural complexities of metal–metalloid nanoparticles: The case of Ni · B as catalyst. *Chem. Eur. J.* **15**, 1134–1143 (2009).

[28] Jamet, S. *et al.* Quantitative analysis of shadow X-ray magnetic circular dichroism photoemission electron microscopy. *Phys. Rev. B* **92**, 144428 (2015). URL http://link.aps.org/doi/10.1103/PhysRevB.92.144428.

[29] Khvalkovskiy, A. V. *et al.* Matching domain-wall configuration and spin-orbit torques for efficient domain-wall motion. *Phys. Rev. B* **87**, 020402 (2013). URL https://link.aps.org/doi/10.1103/PhysRevB.87.020402.

[30] O'Handley, R. C. *Modern magnetic materials* (Wiley, 2000).

[31] Locatelli, A. & Bauer, E. Recent advances in chemical and magnetic imaging of surfaces and interfaces by XPEEM. *J. Phys. Condens. Matter* **20**, 093002 (2008). URL http://stacks.iop.org/0953-8984/20/i=9/a=093002.

[32] Cheng, X. M. & Keavney, D. J. Studies of nanomagnetism using synchrotron-based X-ray photoemission electron microscopy (X-PEEM). *Rep. Prog. Phys.* **75**, 026501 (2012).

[33] Fischer, P. & Ohldag, H. X-rays and magnetism. *Rep. Prog. Phys.* **78**, 094501 (2015). URL http://stacks.iop.org/0034-4885/78/i=9/a=094501.

[34] Stöhr, J. & Siegmann, H. *Magnetism: From Fundamentals to Nanoscale Dynamics*, vol. 152 of *Springer Series in Solid-State Sciences*, chap. 9–10 (Springer, 2006).

[35] Alouges, F., Kritsikis, E., Steiner, J. & Toussaint, J.-C. A convergent and precise finite element scheme for Landau–Lifschitz–Gilbert equation. *Numer. Math* **128**, 407–430 (2014).

[36] http://feellgood.neel.cnrs.fr.

[37] Nakajima, R., Stöhr, J. & Idzerda, Y. Electron-yield saturation effects in L-edge X-ray magnetic circular dichroism spectra of Fe, Co, and Ni. *Phys. Rev. B* **59**, 6421 (1999).

ACKNOWLEDGEMENTS

The autors thank to Márlio Bonfim and Jan Vogel for help with focused MOKE setup, Ségolène Jamet for discussions on simulations and XMCD-PEEM simulation code; Daria Gusakova for unroll-tube script and discussion on micromagnetic simulations; Prof. Christina Trautmann (GSI Helmholtzzentrum for Heavy Ion Research) for the support with irradiation experiments for the template synthesis.

The authors acknowledge Elettra and Soleil synchrotron facilities for allocating beamtime for the XPEEM and STXM experiments and namely Sufal Swaraj, Stefan Stanescu and Adrien Besson for STXM preparations (magnet, software, setup, . . .).

M.S. acknowledges grant from the Laboratoire d'excellence LANEF in Grenoble (ANR-10-LABX-51-01). S.S. gratefully acknowledge funding by the LOEWE project RESPONSE of the Hessen State Ministry of Higher Education, Research and the Arts (HMWK).

AUTHOR CONTRIBUTIONS

- S.S. and W.E. fabricated the samples and M.S. prepared them for measurements.
- L.C. did the transmission electron microscopy imaging. E.G. performed scanning transmission electron microscopy and chemical analysis (EELS).
- J.C.T. developed the code for XMCD-PEEM simulations.
- M.S., S.S., A.W., M.R., R.B., A.S., T.O.M., A.L., B.T., S.B., and O.F performed synchrotron XMCD-PEEM imaging.
- M.S., A.W., M.R., R.B., S.M., and O.F. conducted the synchrotron STXM imaging.
- M.S. performed micromagnetic and XMCD-PEEM simulations, focused MOKE, magnetometry, electron microscopy+chemical analysis (EDX)
- M.S., A.W., and O.F. analysed and interpreted the data.
- M.S. and O.F. wrote the paper with contributions from S.S. and A.W.
- O.F. designed the project and supervised the work.